processes

MDPI

Article

Surface Topography Analysis and Surface Roughness Prediction Model of Diamond Wire-Sawed NdFeB Magnet Based on Optimized Back Propagation Neural Network

Guanzheng Li [1], Xingchun Zhang [1], Yufei Gao [1,2,3,*], Fan Cui [1] and Zhenyu Shi [4]

[1] Key Laboratory of High Efficiency and Clean Mechanical Manufacture of MOE, School of Mechanical Engineering, Shandong University, Jinan 250061, China
[2] State Key Laboratory of Advanced Equipment and Technology for Metal Forming, Shandong University, Jinan 250061, China
[3] Shandong Key Laboratory of High Performance Tools and System, Shandong University, Jinan 250061, China
[4] School of Mechanical Engineering, Hebei University of Technology, Tianjin 300401, China
* Correspondence: yfgao@sdu.edu.cn

Abstract: Wire sawing is an important process in the cutting of NdFeB magnets and the sawed surface topography and surface roughness (SR) are important indicators for assessing surface quality. This paper analyzed the effects of process parameters on the sawed NdFeB surface topography and SR based on orthogonal experiments and then presented an SR prediction model called ISSA-BP, which was based on a BP neural network using an improved sparrow search algorithm (ISSA). For the problem of insufficient optimization capability of the traditional sparrow search algorithm (SSA), Cubic chaotic mapping, Latin hypercube sampling, the sine–cosine algorithm, Levy flight, and Cauchy mutation were introduced to improve the traditional sparrow search algorithm (SSA) to obtain ISSA, improving algorithm convergence speed and global optimization. The ISSA was then used to optimize the initial weights and thresholds of the BP neural network for predicting *R*a. Research shows that the sawed surface topography reflects a combination of brittle and ductile material removal. As the workpiece feed speed and size decrease and the wire speed increases, there is a reduction in SR. Compared with the SSA-BP and traditional BP models, the ISSA-BP prediction model has reduced various error indicators such as mean absolute error (MAE) and mean square error (MSE). The mean absolute error (MAE) of the prediction model optimized by the ISSA is 0.064475, the mean square error (MSE) is 0.0072297, the root mean square error (RMSE) is 0.085028, and the mean absolute percentage error (MAPE) is 3.7171%. The research results provide an experimental basis and technical support for predicting the SR and optimizing the process parameters in diamond wire-sawing NdFeB.

Keywords: NdFeB; diamond wire sawing; surface topography; surface roughness; BP neural network; improved sparrow search algorithm

check for updates

Academic Editors: Shahrokh Hatefi, Yimesker S. Yihun and Farouk Smith

Received: 24 January 2025
Revised: 10 February 2025
Accepted: 12 February 2025
Published: 15 February 2025

Citation: Li, G.; Zhang, X.; Gao, Y.; Cui, F.; Shi, Z. Surface Topography Analysis and Surface Roughness Prediction Model of Diamond Wire-Sawed NdFeB Magnet Based on Optimized Back Propagation Neural Network. *Processes* **2025**, *13*, 546. https://doi.org/10.3390/pr13020546

Copyright: © 2025 by the authors. Licensee MDPI, Basel, Switzerland. This article is an open access article distributed under the terms and conditions of the Creative Commons Attribution (CC BY) license (https://creativecommons.org/licenses/by/4.0/).

1. Introduction

The third generation of rare earth permanent magnetic material NdFeB is widely used in electronics, medical machinery, aerospace, and other fields because of its higher magnetic energy product, coercivity, and energy density [1–4]. In different application areas, NdFeB first needs to be cut to fit the specific size requirements. In recent years, the diamond wire saw (DWS) has gradually become the mainstream cutting method for NdFeB due to its advantages such as low kerf loss and friendly processing environment [5,6].

NdFeB magnetic materials generally need to be ground after being sawed to meet the requirements of the subsequent electroplating process. As a key index of surface quality, SR directly affects the workload and cost of the subsequent grinding process, so optimizing SR is of great significance to improve the surface quality and reduce the processing cost. In the DWS processing process, SR is related to the processing parameters. Many scholars have indicated that the feed speed and wire speed are closely related to SR [7–9]. In addition, when the workpiece size changes, the cooling, lubrication, and chip removal effects of the coolant in the narrow cutting gap also change, which in turn affects the surface quality of the sawing process [10]. Therefore, analyzing the mapping relationship between these parameters and SR, and determining suitable processing parameters, is particularly important for improving surface quality.

Due to the important role of SR in evaluating surface quality, scholars have focused on researching the relationship between SR and process parameters. Some researchers have attempted to establish mathematical models based on the machining mechanism and material removal mechanism for SR prediction. Azami et al. [11] established a theoretical prediction model for *Ra* of 316L stainless steel during rotary abrasive finishing based on the material removal mechanism and validated the accuracy of the model through experiments using response surface methodology. Jia et al. [12] developed an *Ra* prediction model for brittle materials in turning fluorophlogopite and ZrO2, based on the theories of fracture mechanics and tribology. Jing et al. [13] proposed an *Ra* prediction model for micro-end-milling of Al6061 material by considering the tool geometry and cutting parameters. Li et al. [14] and Zhu et al. [15] established theoretical prediction models for SR of diamond wire sawing of photovoltaic polycrystalline silicon and sapphire, respectively, based on the theory of indentation fracture mechanics. The effect of machining parameters on SR was also investigated.

Theoretical modeling often involves making idealized assumptions about certain factors that are difficult to account for during the design process, which can impact the accuracy of the final predictions. Compared to theoretical modeling of SR based on machining mechanisms and tool morphology simulation, experimental research offers more direct empirical evidence, which can better guide practical applications and solve practical problems. Therefore, researchers have focused on establishing reliable input–output *Ra* prediction models based on actual machining experimental data. As a statistical tool, regression analysis is widely used to estimate the relationships between the parameters that affect the machining process. Upadhyay et al. [16] developed a multivariate regression model for predicting the turning SR of Ti-6Al-4V alloys based on experimental parameters and good prediction accuracy (maximum percentage error: 7.45%) was achieved. Ozturk et al. [17] obtained a regression prediction model for the SR of sawn wafers with better accuracy and optimal experimental parameters by comparing different linear and nonlinear regression models. However, due to the variation in the functions chosen when using regression models, the predicted results differ significantly, leading to considerable discrepancies in accuracy. Consequently, artificial neural network (ANN) prediction methods based on software calculations have gained popularity in recent years. The back propagation (BP) neural network is a multilayer feedforward neural network trained by an error back propagation algorithm. It has been widely used in signal processing, time series prediction, and other fields because of its powerful nonlinear modeling capability, high flexibility, and adaptive ability. Therefore, scholars have studied the *Ra* prediction model based on the BP neural network. Kayabasi et al. [18] established a model based on the BP neural network to model the relationship between input parameters (wire speed, feed speed, and oil ratio in the coolant) and output values (*Ra*) in DWS cutting of silicon ingots and explored the law of the influence of single-parameter variations on *Ra* through the model. Aiyar et al. [19]

used a back propagation artificial neural network model to predict the *Ra* of the EDM wire-cutting process and the results show that the overall regression value R obtained is 0.94, which indicates that the model has high prediction accuracy. Paturi et al. [20] modeled and predicted the SR *Ra* of Inconel 718 alloy EDM wire-cut machining using a BP neural network model and the results showed that the prediction model has a small prediction error.

However, with the continuous application and research of BP neural networks, it is found that the model exhibits problems such as slow learning convergence and the fact that it is easy for it to fall into local optimal solutions during the training phase, which is mainly due to the fact that the initial weights and thresholds between the input, hidden, and output layers of the model are randomly generated. Therefore, scholars have optimized it by combining various intelligent algorithms to improve the prediction accuracy. Boga et al. [21] used the genetic algorithm (GA) to optimize a BP neural network and developed an ANN-GA network model to predict milling SR and give optimal technology parameters. Yang et al. [22] proposed an ARIMA-SA-BPNN neural network prediction model for network traffic prediction by optimizing the initial weights of the BP neural network through a simulated annealing algorithm (SA) combined with an autoregressive moving average model (ARMA). The results show that its high prediction accuracy is verified by comparing it with traditional flow prediction models. Liu et al. [23] used GA and the particle swarm optimization algorithm (PSO) to optimize the weights and thresholds of the BP neural network, respectively, and compared and analyzed the prediction results with those of the traditional Kriging method and Yang Chizhong filter estimation method. The results showed that the PSO-BP neural network is obviously superior to the other methods, with higher accuracy of data prediction and a better fitting effect. Cui et al. [24] analyzed the influencing factors of aerodynamic pressure amplitude in tunnels, proposed a pressure amplitude prediction model based on the PSO-BP neural network, and determined the optimal parameters of the model using the K-fold cross-validation method, which finally confirmed the optimization effect of PSO on the BP neural network. Wang et al. [25] optimized a BP neural network based on the sparrow search algorithm (SSA) to predict the thermal performance of green roofs in the subtropical region and verified that the prediction model has higher prediction accuracy compared to the traditional BP neural network model through twelve evaluation metrics, such as mean square error (MSE) and root mean square error (RMSE). Yu et al. [26] fused logical chaos mapping and Levy flight strategy into the SSA to enhance the global spatial search capability of the algorithm and used the improved SSA to optimize the initial weights and thresholds of the BP neural network to achieve the prediction of Day-Ahead Wind Power (DAWP). Zheng et al. [27] improved the SSA using sinusoidal chaotic mapping to improve the initial population quality and established the sine–SSA–BP model to solve the optimal solution of the neural network weights and thresholds, which improved the prediction accuracy and stability. Although many scholars have conducted a lot of research in this area, there is still a gap in the study of using hybrid optimization algorithms to predict the SR of NdFeB magnetic materials cut by a diamond wire saw.

This study first conducted NdFeB sawing experiments based on orthogonal testing and analyzed the effects of various process parameters on the sawed surface morphology and SR. Then, the experimental data were used in the dataset for the neural network training and the basic structure of the BP neural network was constructed. Cubic chaotic mapping, Latin hypercube sampling, sine–cosine algorithm, Levy flight, and Cauchy mutation were incorporated into the sparrow search algorithm (SSA) for improvement, resulting in the proposed improved sparrow search algorithm (ISSA). Multiple sets of test functions were selected to compare the performance of the ISSA with that of GA, SA, and PSO algorithms,

validating that the proposed algorithm demonstrates superior convergence ability. Finally, the ISSA was utilized to optimize the BP neural network, establishing a prediction model called ISSA-BP based on the ISSA. Prediction comparison experiments were conducted between the ISSA-BP, SSA-BP, and traditional BP neural networks. By comparing the mean square error, root mean square error, and other metrics among the three models, the effectiveness of the ISSA-BP model in enhancing prediction accuracy was validated. The research results provide experimental evidence and technical support for the prediction of SR and the optimization of process parameters in the processing of NdFeB materials using a diamond wire saw.

2. Materials and Methods

2.1. Experimental Equipment

The cutting experiment was conducted on a single-wire diamond wire-cutting machine (SH300, Guangzhou Shenghai Electronic Technology Co., Ltd, Guangzhou, China). The electron microscope image of the diamond wire (Provided by Shantian New Materials Co., Ltd., Linyi, China) used is shown in Figure 1 and the parameters are listed in Table 1. The schematic diagram of the machine setup is shown in Figure 2d. After passing through the tension wheel and guide wheel, the wire is evenly wrapped around the driving wheel and the tension force of the wire is provided by the heavy object pulling the tension wheel. The section of the wire between the guide pulleys is used for cutting. Before the experiment, the workpiece was fixed on the load table with AB glue, and the cutting position was adjusted by controlling the movement and rotation of the load table. The cutting thickness was set to 1 mm. At the beginning of cutting, the machine motor drove the load table to move in the direction perpendicular to the wire movement at a constant feed speed of V_f, while the wire reciprocated at a speed of V_s for cutting processing. Tap water was chosen as the cutting fluid, which plays a role in lubrication, cooling, and chip removal.

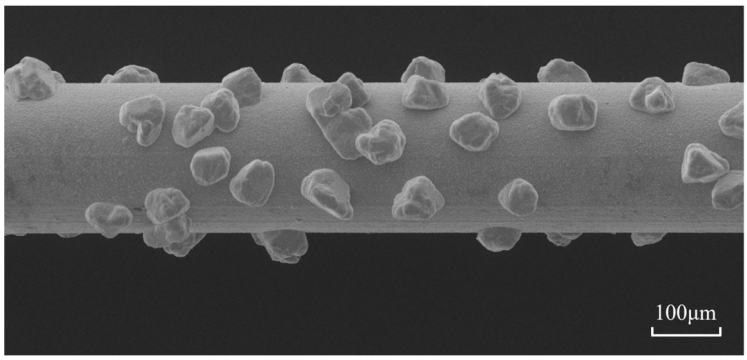


Figure 1. Scanning electron microscopy image of the diamond wire.

Table 1. Saw wire parameters.

Parameters	Parameter Value
Diamond saw wire length (m)	70
Saw wire core diameter (μm)	220
Type of abrasive grain	Surface nickel diamond plated (25% weight gain)
Abrasive grain size (μm)	40–50
Abrasive grain distribution density (grits/mm^2)	70–85
Tensile limit of saw wire (MPa)	3275

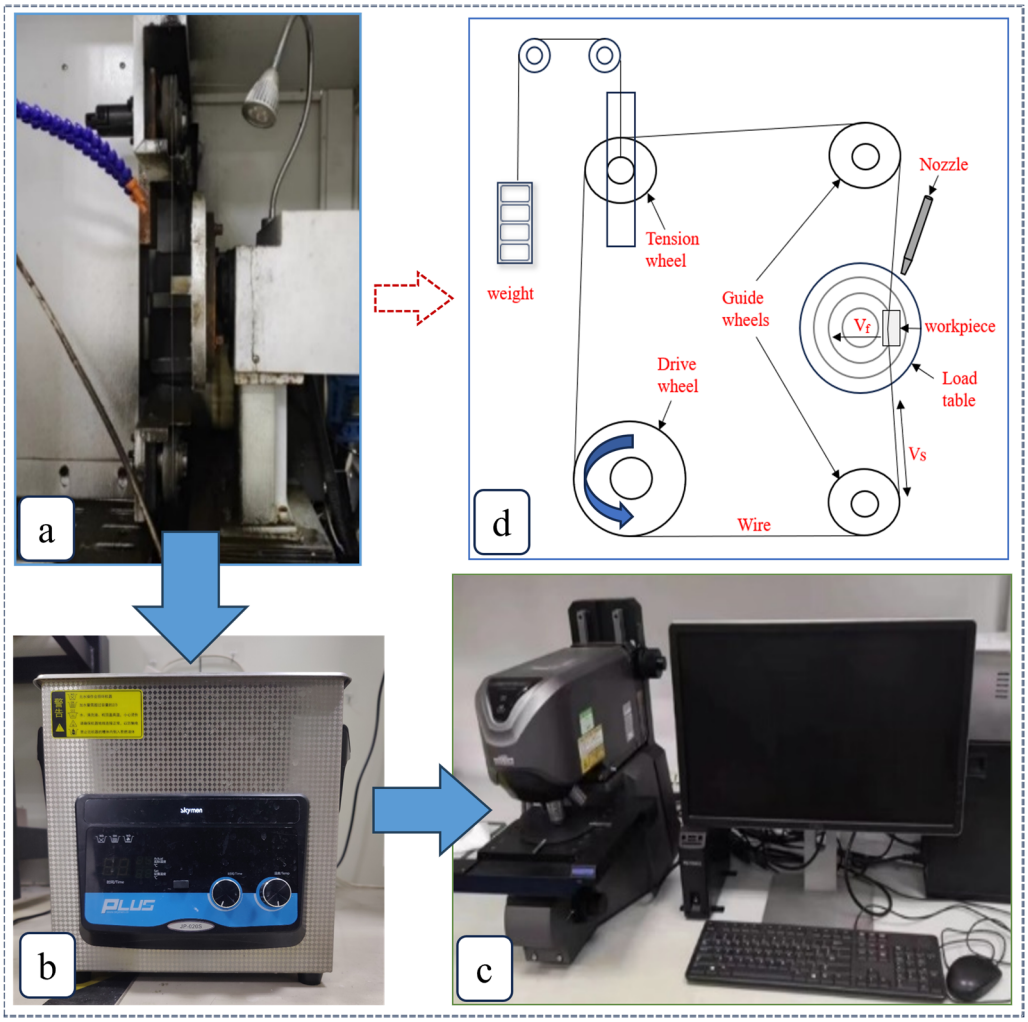


Figure 2. Experimental flowchart. (**a**) Experimental equipment diagram. (**b**) Ultrasonic cleaning machine. (**c**) Keyence 3D laser scanning microscope. (**d**) Sawing schematic.

2.2. Experimental Methods

Previous studies have shown that feed speed (V_f), wire speed (V_s), and workpiece size (s) have significant effects on the SR [10]. Therefore, these three processing parameters were set as variable factors in the experiment, with five levels for each factor. Based on the range of process parameters used in actual industrial production, the five feed speed levels were set as A_1: 0.1 mm/min, A_2: 0.4 mm/min, A_3: 0.7 mm/min, A_4: 1.0 mm/min, and A_5: 1.3 mm/min. The five wire speed levels were B_1: 800 m/min, B_2: 1000 m/min, B_3: 1200 m/min, B_4: 1400 m/min, and B_5: 1600 m/min. The five workpiece sizes were C_1: 10 mm, C_2: 20 mm, C_3: 30 mm, C_4: 40 mm, and C_5: 50 mm, varied in the dimension perpendicular to the wire's feed direction. This forms a three-factor, five-level orthogonal experiment. The specific parameter combinations are shown in Table 2. To expand the database and improve the stability of the prediction model, 17 additional experiments were conducted based on the orthogonal experiments, resulting in a total of 42 experimental datasets for neural network training and testing.

After processing, each sample was cleaned using an ultrasonic cleaner (Skymen Shenzhen Jiemeng Technology Co., Shenzhen, China) and the surface morphology was observed with a Keyence 3D laser scanning microscope VK-X200K (Keyence Corporation, Osaka, Japan). The *Ra* along the workpiece feed direction was measured, with five stable cutting areas selected from each sample for measurement, and their average was taken as the final result. The experimental process flowchart is shown in Figure 2.

Table 2. Orthogonal experimental parameter combination table.

No.	Combination			No.	Combination		
1	A_1	B_1	C_1	14	A_3	B_4	C_5
2	A_1	B_2	C_3	15	A_3	B_5	C_2
3	A_1	B_3	C_5	16	A_4	B_1	C_3
4	A_1	B_4	C_2	17	A_4	B_2	C_5
5	A_1	B_5	C_4	18	A_4	B_3	C_2
6	A_2	B_1	C_5	19	A_4	B_4	C_4
7	A_2	B_2	C_2	20	A_4	B_5	C_1
8	A_2	B_3	C_4	21	A_5	B_1	C_2
9	A_2	B_4	C_1	22	A_5	B_2	C_4
10	A_2	B_5	C_3	23	A_5	B_3	C_1
11	A_3	B_1	C_4	24	A_5	B_4	C_3
12	A_3	B_2	C_1	25	A_5	B_5	C_5
13	A_3	B_3	C_3				

2.3. Experimental Results and Analysis

The *Ra* values obtained from the experiment are shown in Table 3, which serve as the dataset for training and testing the artificial neural network prediction model proposed in this paper. Among them, the first 25 sets come from the orthogonal experiments. The training set consists of 35 sets, and the test set consists of 7 sets, with 'a' in Table 3 representing the test set data for the model.

Figure 3 shows the 2D sawed surface morphology at a wire speed of V_s = 1200 m/min and a workpiece size of s = 30 mm, with feed speeds of 0.1 mm/min ($A_1B_3C_3$) and 1.3 mm/min ($A_5B_3C_3$), respectively. The white areas represent the ductile removal regions, and the black areas represent the brittle removal regions. Material removal during diamond wire saw cutting is realized by diamond abrasives fixed on the wire surface pressing into and scratching the workpiece surface with the movement of the wire. The material removal process, however, is a combination of ductile removal and brittle fracture, which is largely dependent on the processing conditions. Considering the differences in the form and dimensions of the diamond abrasives on the wire, as well as the different protrusion heights of the abrasives, the stress conditions at the contact points between the abrasives and the workpiece also varied, leading to randomness in the material removal mode. This is reflected in the figure, where the sawed surface showed the combined effects of brittle and ductile removal. As shown in Figure 3, at a feed speed of 0.1 mm/min, the white area occupied a larger proportion, with ductile removal being the dominant material removal mode. When the feed speed increases to 1.3 mm/min, the proportion of black brittle removal areas significantly increased, and the form and dimensions of brittle pits also increased, resulting in a decline in surface quality.

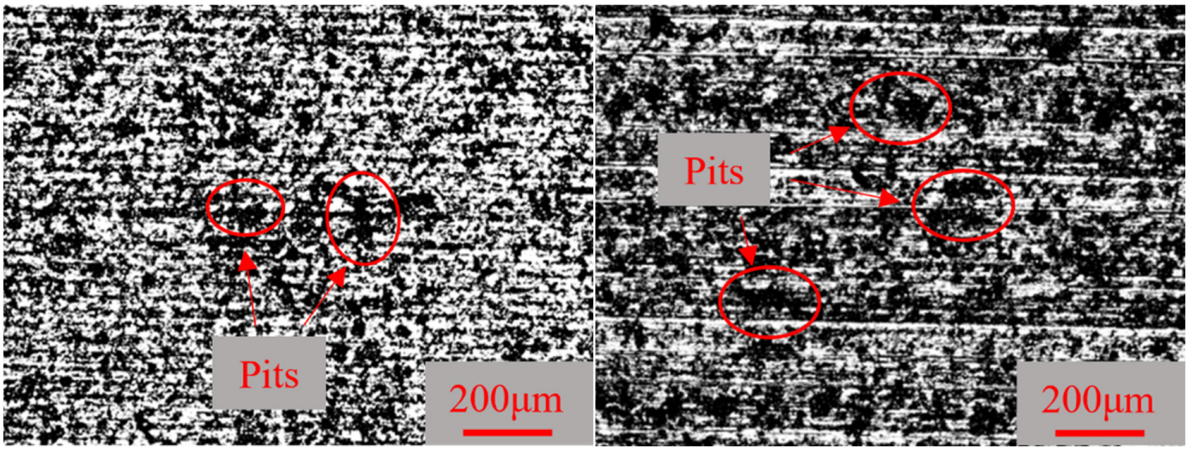
In order to adapt to the single-factor increase in feed speed, the material removal rate per unit of time increased, which required a corresponding increase in the cutting depth of the diamond abrasives on the wire. When the cutting depth exceeded the depth threshold of the brittle–ductile transition, the material removal mode shifted from ductile removal to brittle removal, accompanied by the formation of median cracks and lateral cracks [28,29]. As the cutting depth further increased, the size of median and lateral cracks also expanded, which specifically manifested as an increase in the dimensions and number of brittle pits.

Table 3. Experimental data.

No.	Combination	V_f (mm/min)	V_s (m/min)	s (mm)	Ra (μm)
1	$A_1B_1C_1$	0.1	800	10	0.634
2[a]	$A_1B_2C_3$	0.1	1000	30	0.679
3	$A_1B_3C_5$	0.1	1200	50	0.732
4	$A_1B_4C_2$	0.1	1400	20	0.522
5	$A_1B_5C_4$	0.1	1600	40	0.579
6	$A_2B_1C_5$	0.4	800	50	2.382
7	$A_2B_2C_2$	0.4	1000	20	1.281
8[a]	$A_2B_3C_4$	0.4	1200	40	1.387
9[a]	$A_2B_4C_1$	0.4	1400	10	0.964
10	$A_2B_5C_3$	0.4	1600	30	1.129
11[a]	$A_3B_1C_4$	0.7	800	40	3.489
12	$A_3B_2C_1$	0.7	1000	10	2.247
13	$A_3B_3C_3$	0.7	1200	30	2.094
14	$A_3B_4C_5$	0.7	1400	50	2.051
15	$A_3B_5C_2$	0.7	1600	20	1.512
16	$A_4B_1C_3$	1.0	800	30	4.416
17[a]	$A_4B_2C_5$	1.0	1000	50	3.875
18	$A_4B_3C_2$	1.0	1200	20	2.378
19	$A_4B_4C_4$	1.0	1400	40	2.501
20	$A_4B_5C_1$	1.0	1600	10	1.720
21	$A_5B_1C_2$	1.3	800	20	4.847
22	$A_5B_2C_4$	1.3	1000	40	4.319
23[a]	$A_5B_3C_1$	1.3	1200	10	2.979
24	$A_5B_4C_3$	1.3	1400	30	2.732
25	$A_5B_5C_5$	1.3	1600	50	3.263
26	$A_1B_3C_3$	0.1	1200	30	0.598
27	$A_2B_3C_3$	0.4	1200	30	1.296
28	$A_4B_3C_3$	1.0	1200	30	2.629
29	$A_5B_3C_3$	1.3	1200	30	3.583
30	$A_3B_1C_3$	0.7	800	30	3.319
31	$A_3B_2C_3$	0.7	1000	30	2.589
32	$A_3B_4C_3$	0.7	1400	30	1.898
33[a]	$A_3B_5C_3$	0.7	1600	30	1.592
34	$A_3B_3C_1$	0.7	1200	10	1.847
35	$A_3B_3C_2$	0.7	1200	20	1.913
36	$A_3B_3C_4$	0.7	1200	40	2.337
37	$A_3B_3C_5$	0.7	1200	50	2.597
38	$A_3B_5C_1$	0.7	1600	10	1.303
39	$A_5B_1C_3$	1.3	800	30	5.015
40	$A_1B_5C_3$	0.1	1600	30	0.489
41	$A_3B_1C_5$	0.7	800	50	3.673
42	$A_1B_5C_1$	0.1	1600	10	0.433

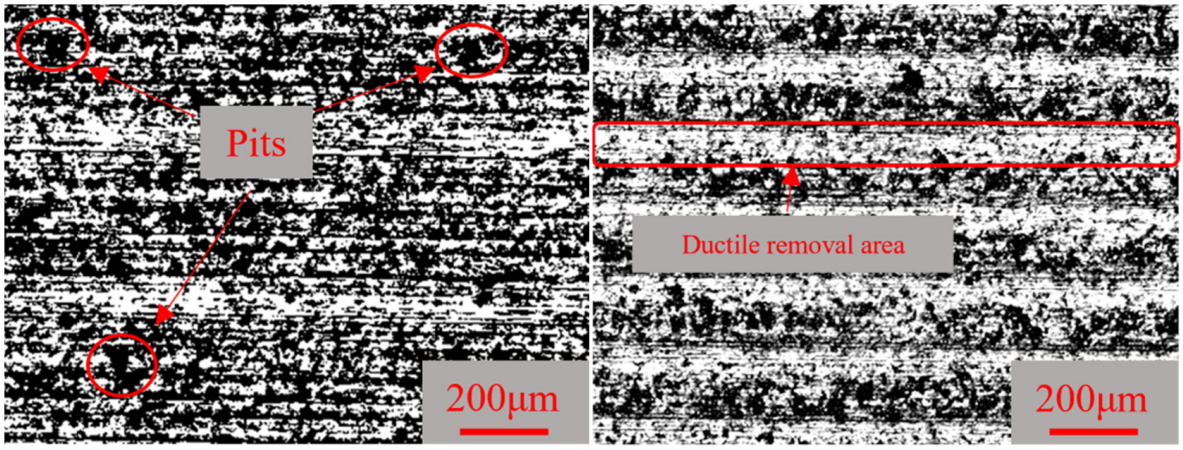
Figure 4 shows the 2D surface morphology of the sawed surface at a feed speed of V_f = 0.7 mm/min and a workpiece size of s = 30 mm, with wire speeds of 800 m/min ($A_3B_1C_3$) and 1600 m/min ($A_3B_5C_3$), respectively. It can be seen from Figure 4a that a large number of black brittle pits appeared on the sawed surface, which means that at a wire speed of 800 m/min, the material removal mode on the sawed surface was still predominantly brittle removal. When the wire speed increased to 1600 m/min, the number and size of brittle pits on the sawed surface decreased, and the white ductile removal areas increased, indicating that the material removal mode in more regions shifted from brittle removal to ductile removal. When the wire speed increased as a single factor,

the contact frequency between the abrasives and the sawing points increased, with more abrasives participating in the process per unit time. However, since the feed speed remained unchanged, the material removal rate per unit time did not change. The involvement of more abrasives meant that each abrasive had a smaller average cutting depth, making it difficult to reach the brittle–ductile transition threshold. This was reflected in the surface morphology as an increase in the area of ductile removal bands and a reduction in the number and volume of brittle pits. This pattern was also found in the cutting of silicon carbide [30] and sapphire materials [31].



(**a**) V_f = 0.1 mm/min. (**b**) V_f = 1.3 mm/min.

Figure 3. Surface morphology of slices at different feed speeds (V_s = 1200 m/min, s = 30 mm).

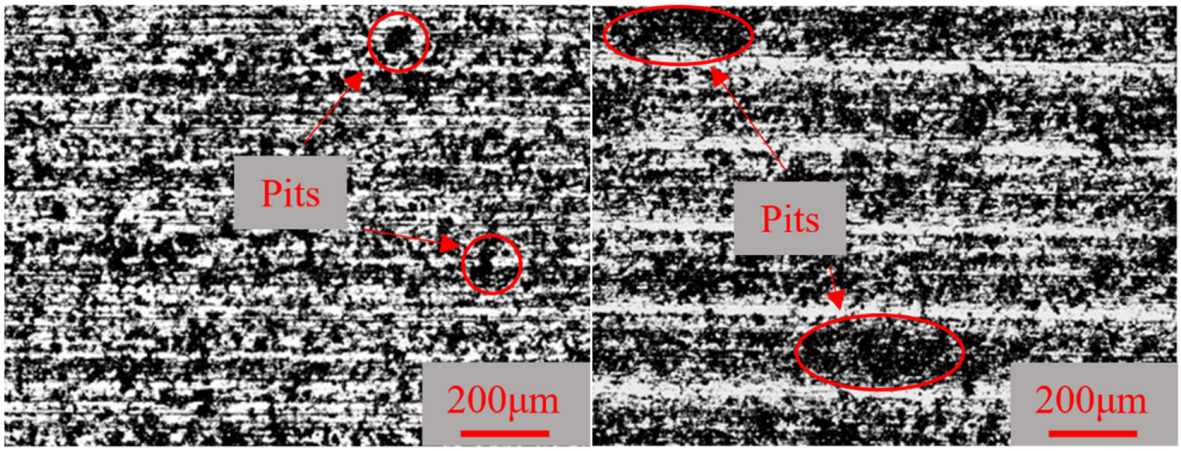


(**a**) V_s = 800 m/min. (**b**) V_s = 1600 m/min.

Figure 4. Surface morphology of slices at different wire speeds (V_f = 0.7 mm/min, s = 30 mm).

Figure 5 shows the 2D surface morphology of the sawed surface at a feed speed of V_f = 0.7 mm/min and a wire speed of V_s = 1200 m/min, with workpiece sizes of 10 mm ($A_3B_3C_1$) and 50 mm ($A_3B_3C_5$), respectively. It can be seen from the figure that different workpiece sizes have a certain impact on the surface morphology of the sawing process. As shown in Figure 5b, when the workpiece size increased from 10 mm to 50 mm, the area of brittle removal regions on the sawed surface increased, and the size and number of brittle pits also grew, accompanied by a clustering phenomenon. The change in workpiece size directly affected the effective cutting length of the abrasives. As the effective cutting length increased, chip removal became more difficult. More and more chips, accompanied by detached abrasive particles, accumulated in the kerf and could not be discharged, causing secondary grinding on the surface driven by the wire. This increased the cutting depth

and raised the proportion of brittle removal regions. In areas with severe accumulation, the surface exhibited clustered brittle pits. It is worth noting that compared with Figure 5a, Figure 5b shows an alternating pattern of brittle and ductile removal regions. Considering the limited amount of chip accumulation in the kerf, once the accumulation reached its limit under the reciprocating motion of the wire, a large amount of chips was quickly released along the wire movement direction, resulting in a rapid reduction in cutting depth and the appearance of temporary ductile removal regions. In addition, due to the increase in effective processing length, the impact of lubrication and cooling on the surface quality of slices cannot be ignored [10].



(**a**) S = 10 mm. (**b**) S = 50 mm.

Figure 5. Surface morphology of slices at different workpiece sizes (V_f = 0.7 mm/min, V_s = 1200 m/min).

It is necessary to further analyze the effects of various process parameters on SR. The signal-to-noise ratio (S/N) is a key metric for assessing data variation and is widely used in the analysis of surface quality during processing [32,33]. Depending on the experimental objectives, the signal-to-noise ratio is usually divided into three types: the smaller the better, the larger the better, and the nominal the best state. Since the surface quality evaluation index used in this study is *Ra* value, and a smaller *Ra* value indicates better surface quality, the "smaller the better" type of S/N evaluation indicator was selected. The experimental result data were converted into signal-to-noise ratios according to Equation (1), with a larger signal-to-noise ratio corresponding to a smaller *Ra*.

$$S/N = -10log\left(\frac{1}{n}\sum_{i=1}^{n} {x_i}^2\right) \quad (1)$$

where n represents the experiment number and x_i represents the data of the i-th experiment.

The results of the orthogonal experiment were analyzed using Minitab Statistical Software version 2020 (Minitab, State College, PA, USA). Figure 6 shows the signal-to-noise ratios of *Ra* for the three factors at different levels. It can be seen from the figure that all three factors have some influence on SR. Among them, the variation in *Ra* signal-to-noise ratio caused by changes in feed speed is significantly greater than that of the other two factors, indicating that feed speed is the most influential factor on SR. The variation in *Ra* signal-to-noise ratio caused by changes in workpiece size is the smallest, making it the least influential factor on SR. Additionally, as feed speed and workpiece size increase, the S/N value gradually decreases, indicating an inverse relationship between these two variables and the signal-to-noise ratio. In contrast, as wire speed increases, the S/N value gradually rises, showing a direct relationship between the two. Since the "the smaller the better"

type of S/N was used, a larger S/N value indicates a smaller *Ra* value. Therefore, based on the S/N, it can be determined that both feed speed and workpiece size are directly proportional to SR, while wire speed is inversely proportional to SR. Figure 7 shows the main effects plot of the mean *Ra* for the three factors at different levels. It can be clearly seen from Figure 7 that the *Ra* value gradually increases with the increase in feed speed and workpiece size, while it gradually decreases with the increase in wire speed.

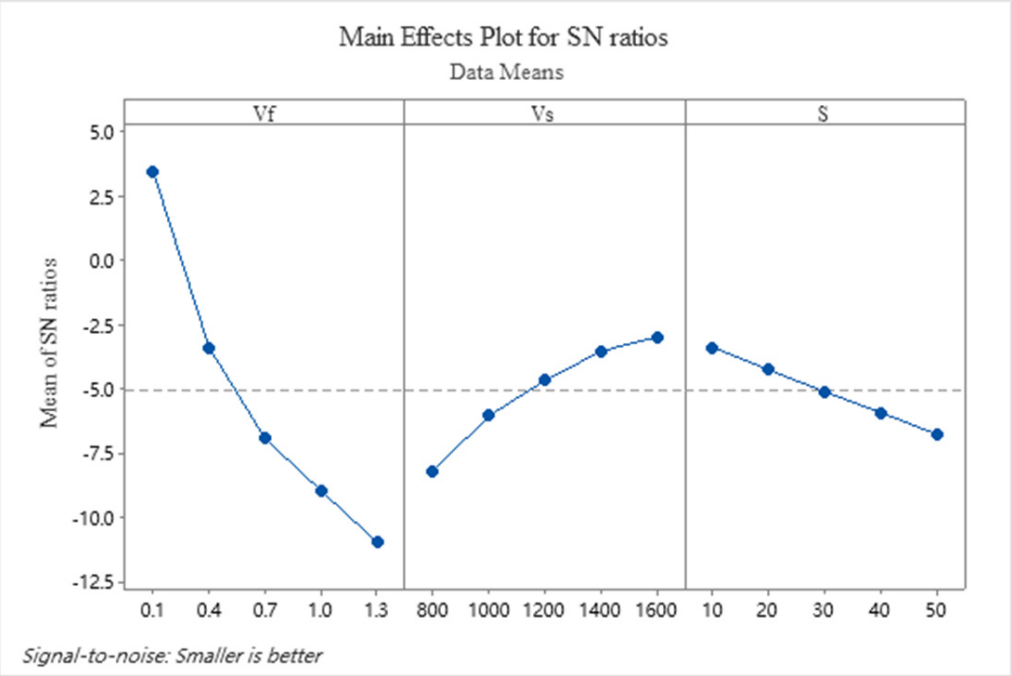


Figure 6. S/N ratio graph of the factor.

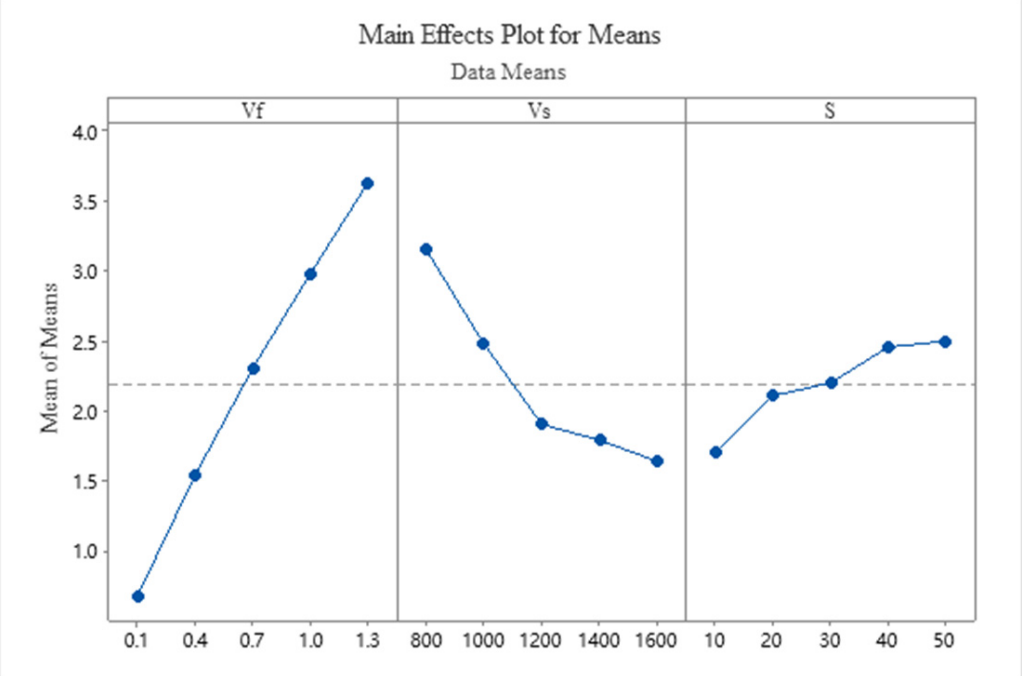


Figure 7. Main effects plot for means.

3. Model Architecture of the ISSA-BP Neural Network

3.1. BP Neural Network Model Structure

The BP neural network model's topology includes one input layer, multiple hidden layers, and a single output layer. The input information is transmitted unidirectionally through the input layer, hidden layers, and output layer. The nodes in consecutive layers are linked by weights according to their influence strength and the weights are continuously updated through back propagation of the error from the output layer. Hornik et al. [34] found that a three-layer neural network can approximate any function, provided the activation function is properly chosen and there are enough hidden layer nodes. Therefore, this paper uses a three-layer neural network structure, which is more convenient for parameter calculation and is widely applied. The network's final output is represented by the following equation:

$$y = F_2\left\{\sum_{j=1}^{n} w_{jk}[F_1(\sum_{i=1}^{m} w_{ij}x_i + b_j)] + b_k\right\} \tag{2}$$

where y is the final output value; x_i is the network input value; m is the number of input layer nodes; n is the number of hidden layer nodes; w_{ij} and w_{jk} are the connection weights between the input and hidden layers, and between the hidden and output layers, respectively; b_j and b_k represent the biases of the hidden and output layer nodes; and F is the activation function. The Sigmoid activation function is applied in the hidden layer, while the purelin function is used in the output layer to accommodate outputs of any size. They are expressed as follows:

$$F_1\left(x\right) = \frac{1}{1+e^{-x}} \tag{3}$$

$$F_2\left(x\right) = x \tag{4}$$

In this study, the evaluation factors are feed speed (V_f), wire speed (V_s), and workpiece size (s), and so the model's input layer was set to three nodes. The output layer represents the Ra value and therefore one output node was set. Research indicates that too few neurons in the hidden layer can prevent achieving training accuracy, whereas too many may result in overfitting [35]. Therefore, the selection of the number of hidden layer nodes is crucial. The number of hidden layer nodes can be determined by the range given by the Kolmogorov theorem [36], as shown in Equation (5).

$$h = \sqrt{m+n} + a \tag{5}$$

where m, h, and n are the numbers of nodes in the input layer, hidden layer, and output layer, respectively, and a is a constant in the range [1,10].

The range of the number of neurons in the hidden layer, determined by this empirical equation, is [3,12]. The number of hidden layer nodes is set to be automatically adjusted, with the goal of minimizing the mean square error (MSE) to determine and select the ideal number of hidden layer neurons. The expression for MSE is shown in Equation (6).

$$MSE = \frac{1}{n}\sum_{i=1}^{n}\left(\hat{y}_i - y_i\right)^2 \tag{6}$$

where n is the number of samples, $\hat{y}_i$ is the predicted value, and y_i is the true value.

Assuming that the maximum number of iterations for the network is set to 1000, the trainlm function is selected as the training function, and the learning rate is set to 0.1.

The MSE function is selected as the error objective function, with the desired error set to 0.1×10^{-3}. Figure 8 shows the schematic diagram of the final neural network structure.

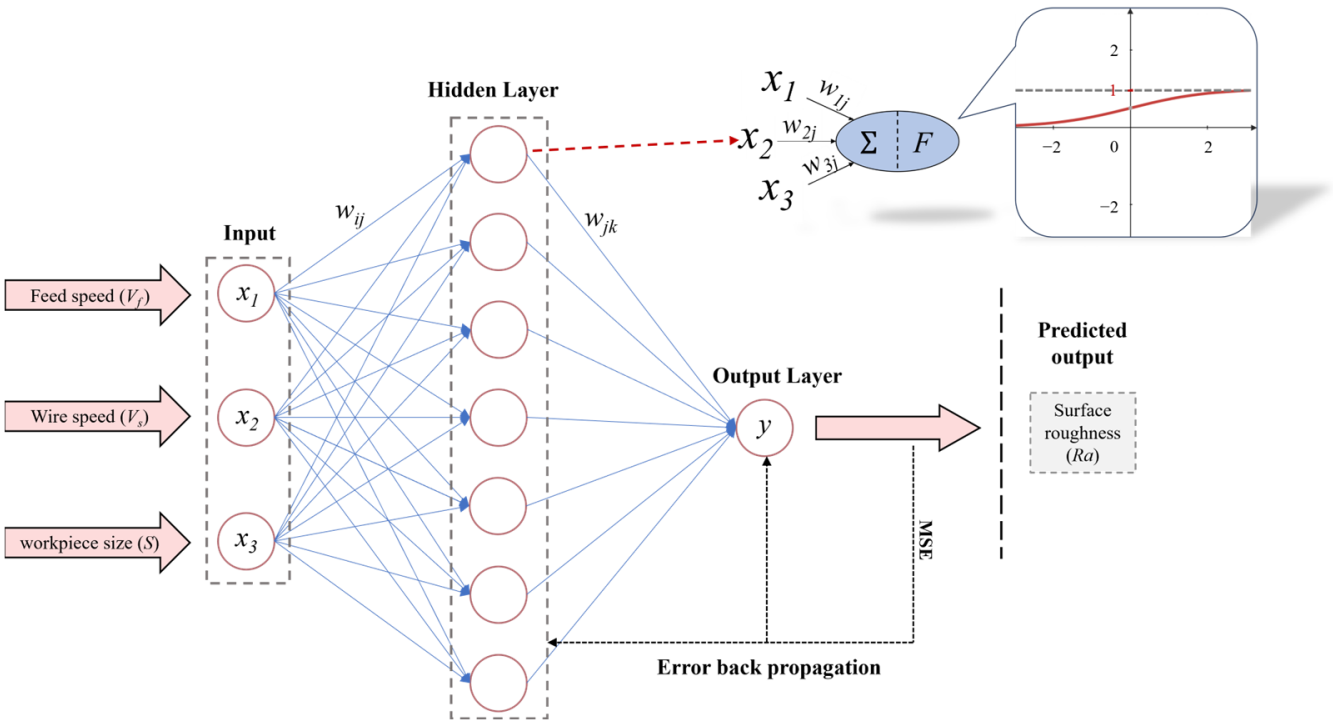


Figure 8. BP neural network structure diagram.

3.2. SSA Optimized by Hybrid Strategy

BP neural networks have strong nonlinear modeling capabilities, but traditional BP neural networks have weak generalization ability and are easily affected by local optima points during the optimization process. Therefore, neural networks often need to be combined with certain algorithms for optimization. The SSA, a heuristic optimization algorithm based on the behavior of sparrow populations, was proposed by Xue et al. [37] in 2020 and has been extensively used for optimizing neural networks. The algorithm can efficiently search the solution space to find the global optimal solution or near-optimal solution by simulating the social behavior of sparrows. Although the SSA is designed to avoid getting trapped in local optima, the SSA may still risk premature convergence to non-global optimal solutions in practice, and needs to be used in combination with other techniques or algorithms to improve the ability of solving problems. Therefore, this paper proposes a mixed-strategy improved SSA called ISSA to address this issue. The flowchart of ISSA is shown in Figure 9, and the specific improvement steps are as follows:

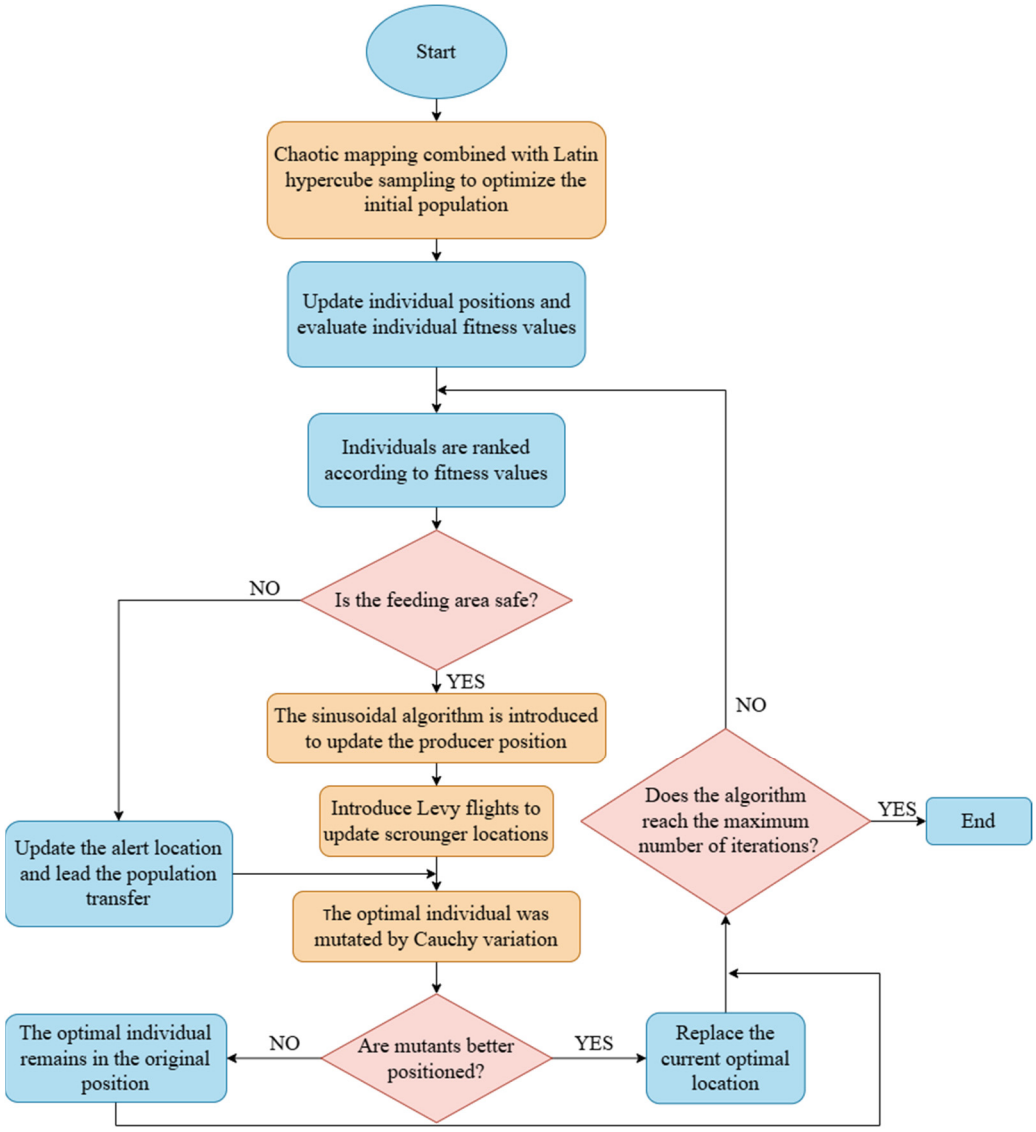


Figure 9. ISSA flowchart.

First, it is necessary to configure the ISSA parameters and initialize the initial population. The SSA typically uses a randomly generated initial population, which results in low population quality and uneven distribution. In this study, Latin hypercube sampling is employed to generate uniformly distributed sample points within the specified search space. These sample points are then processed using Cubic chaotic mapping to further increase their dispersion and randomness. The processed sample points are used as the final initial population, enabling better coverage of the search space and enhancing the global search capability.

In the SSA, the position updates of producers are prone to premature convergence, which can affect the final result [38]. Therefore, the sine–cosine algorithm (SCA) was introduced to update the positions of the producers. The SCA includes some random and adaptive parameters to balance global exploration and local exploitation. The position updating equation for producer individuals during the optimization process is as follows:

$$X_{i,j}^{t+1} = \begin{cases} X_{i,j}^{t} + r_1 \cdot \sin(r_2) \times \left| r_3 \cdot X_{\text{best}} - X_{i,j}^{t} \right|, & R_2 < ST \\ X_{i,j}^{t} + r_1 \cdot \cos(r_2) \times \left| r_3 \cdot X_{\text{best}} - X_{i,j}^{t} \right|, & R_2 \geq ST \end{cases} \quad (7)$$

where t is the current iteration number and $X_{i,j}^{t}$ represents the value of the j-th dimension of the i-th individual in the t-th generation population. X_{best} represents the position of the current optimal individual and r_1 is the switching parameter used to adjust the amplitude of the sine and cosine functions. Its value is $r_1 = a \times (1 - t/T)$, where a is a constant, typically set to 2, and T is the maximum number of iterations; r_2 and r_3 are random numbers following a uniform distribution, where $r_2 \in (0, 2\pi)$, $r_3 \in (0, 2)$. R2($R_2 \in [0, 1]$) and ST ($ST \in [0.5, 1.0]$) represent the alarm value and safety threshold, respectively.

The condition for followers to become producers is that the producers have iterated for a certain number of times and their fitness value no longer changes. To prevent the algorithm from getting trapped in local optima, the Levy flight strategy is incorporated into the follower update equation to improve global search capability. Levy flight is a random walk pattern with a long-tailed distribution, which provides greater jumps compared to traditional random walks and allows for a wider search area in a shorter time [39]. The improved follower position update equation is as follows:

$$X_{i,j}^{t+1} = \begin{cases} Q \cdot \exp\left(\frac{X_{worst}^{t} - X_{i,j}^{t}}{i^2}\right) & \text{if } i > \text{n}/2 \\ X_{p}^{t+1} + X_{p}^{t+1} \otimes \text{Levy}(d) & \text{otherwise} \end{cases} \tag{8}$$

where X_{p}^{t+1} is the optimal position occupied by the current discoverer; Q is a random number following a normal distribution; X_{worst}^{t} represents the current global worst position; t is the number of iterations; d is the vector dimension; and the Levy calculation equation is as follows:

$$Levy(d) = 0.01 \cdot \frac{r_4 \cdot \sigma}{|r_5|^{1/\beta}} \tag{9}$$

$$\sigma = \left\{ \frac{\Gamma(1+\beta) \cdot \sin(\pi\beta/2)}{\Gamma[(1+\beta)/2]\beta \cdot 2^{(\beta-1)/2}} \right\}^{1/\beta} \tag{10}$$

where Γ is the Gamma function; β is a constant, set to 1.5 in this paper; and r_4 and r_5 are random numbers in the range [0, 1].

In addition, a portion of the population is randomly divided as scouts, and their position update equation is shown in Equation (11):

$$X_{i,j}^{t+1} = \begin{cases} X_{\text{best}}^{t} + \beta \cdot \left| X_{i,j}^{t} - X_{\text{best}}^{t} \right| & \text{if } f_i > f_g \\ X_{i,j}^{t} + K \cdot \left(\frac{\left| X_{i,j}^{t} - X_{\text{worst}}^{t} \right|}{(f_i - f_w) + \varepsilon} \right) & \text{if } f_i = f_g \end{cases} \tag{11}$$

where β is a step-size control parameter, a random number following a normal distribution with a mean of 0 and a variance of 1. $K(K \in [-1, 1])$ are random numbers. f_i represents the current fitness value of the sparrow. f_g and f_w denote the current global best and worst fitness values, respectively. ε is a small constant set to 10×10^{-60} to prevent zero division errors.

The Cauchy distribution is a probability distribution with heavier tails compared to the normal distribution. This means that, during the optimization process, using Cauchy mutation may result in larger jumps, which can help escape local optima, increase the diversity of the search space, and prevent getting trapped in local optima [40]. Therefore, in this paper, the Cauchy mutation operator is used to perturb the position of the optimal solution, improving the algorithm's tendency to fall into local regions and enhancing its

global optimization performance. The probability density in one dimension of the Cauchy distribution is as follows:

$$f(x) = \frac{1}{\pi} \cdot \frac{a}{a + x^2}, \ x \in (-\infty, +\infty) \tag{12}$$

When the value of a in Equation (12) is 1, it is called the standard Cauchy distribution (SCD). The perturbation operation equation for the optimal solution position using the SCD is as follows:

$$X_{i,j}^{t+1} = X_{best}(t) + Cauchy(0,1) \oplus X_{best}(t) \tag{13}$$

where *Cauchy* (0,1) represents the SCD, and the Cauchy distribution random variable generation function is $\eta = \tan[(\xi - 0.5)\pi]$.

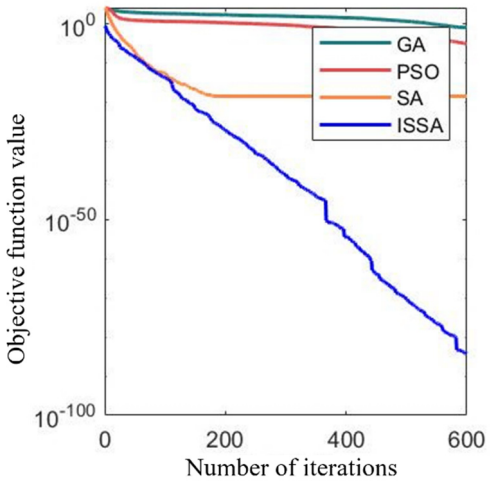
3.3. ISSA Performance Comparison Experiments

To test the performance of the ISSA, the simulated annealing (SA) algorithm, genetic algorithm (GA), particle swarm optimization (PSO), and ISSAs were selected for comparison. All four algorithms were tested under the same general conditions: the population size was set to 30 and the number of iterations was set to 600. The number of producers in the SSA was set to 20% of the total population, with 10% of the sparrows aware of danger (SD), and the safety threshold (ST) was set to 0.8. Eight standard test functions commonly used in optimization algorithm testing were selected, including four unimodal test functions and four multimodal test functions. Unimodal functions possess a single global optimum and are relatively less computationally challenging, utilized to evaluate the algorithm's convergence speed and accuracy. Multimodal test functions possess multiple local optima and require a higher level of global search capability from the algorithm. The two sets of functions are shown in Tables 4 and 5 [41], respectively, which are commonly used reference standards for evaluating algorithm performance. All experiments were conducted in the same environment using MATLAB 2021a. Figure 10 presents the convergence curves of the algorithms.

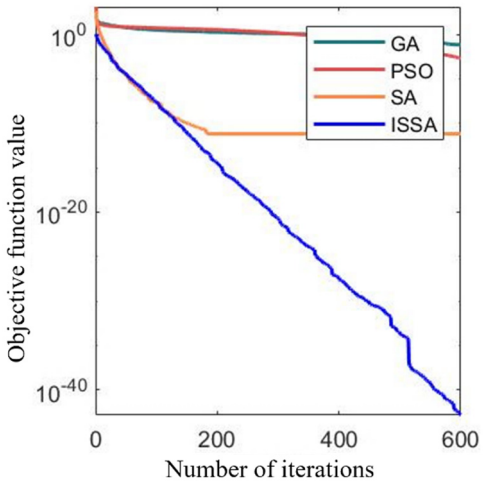
Table 4. Unimodal test function.

Expression	Dimensionality	Initial Range	Theoretical Minimum
$F_1(x) = \sum_{i=1}^{n} {x_i}^2$	30	$[-100, 100]$	0
$F_2(x) = \sum_{i=1}^{n} \lvert x_i \rvert + \prod_{i=1}^{n} \lvert x_i \rvert$	30	$[-10, 10]$	0
$F_3(x) = \sum_{i=1}^{n} \left(\sum_{j=1}^{i} x_j \right)^2$	30	$[-100, 100]$	0
$F_4(x) = \max_i \{ \lvert x_j \rvert, \ 1 \le i \le n \}$	30	$[-100, 100]$	0

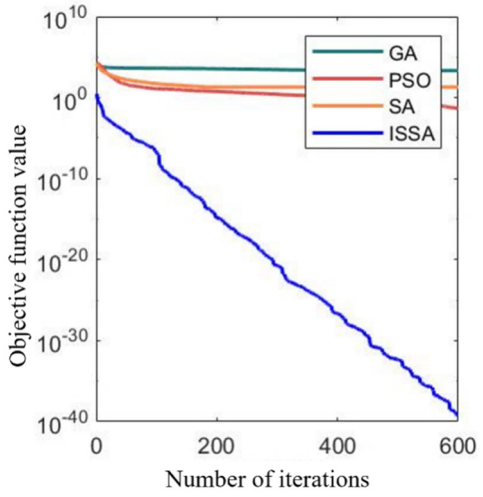
It can be seen from Figure 10 that, whether for unimodal or multimodal functions, the optimization effect of the ISSA is superior to GA, SA, and PSO. ISSA consistently achieved good fitness values at the start and showed faster convergence speed. With the same number of iterations, the solution accuracy of ISSA was also notably higher than that of the other algorithms, demonstrating the superiority of the ISSA.



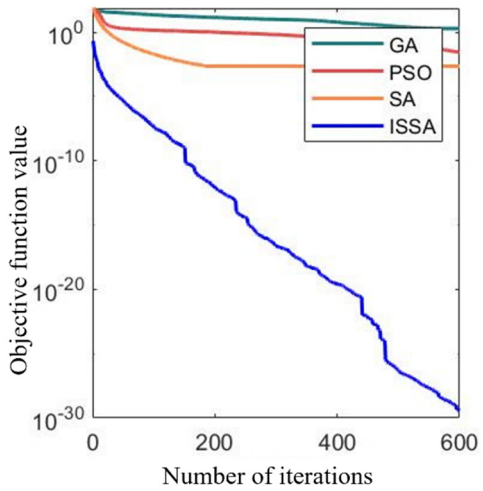
(**a**) Test function F_1.



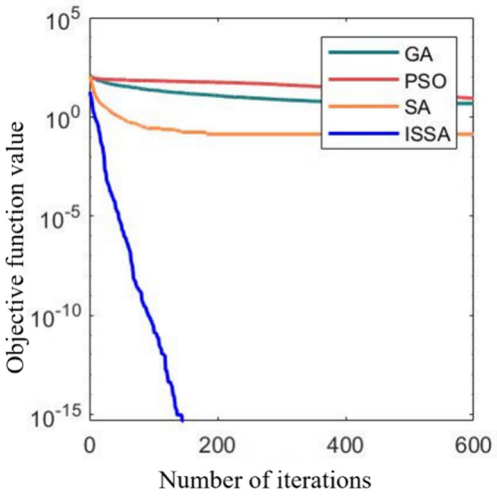
(**b**) Test function F_2.



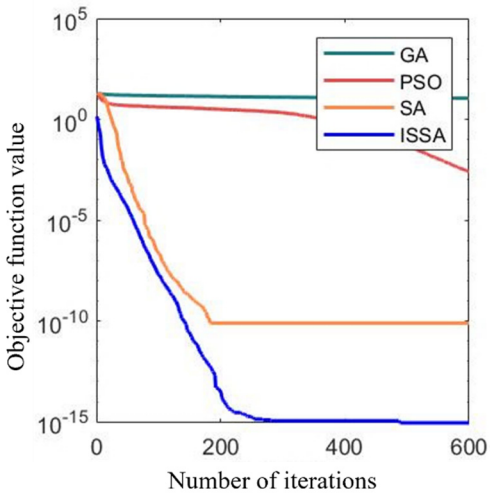
(**c**) Test function F_3.



(**d**) Test function F_4.

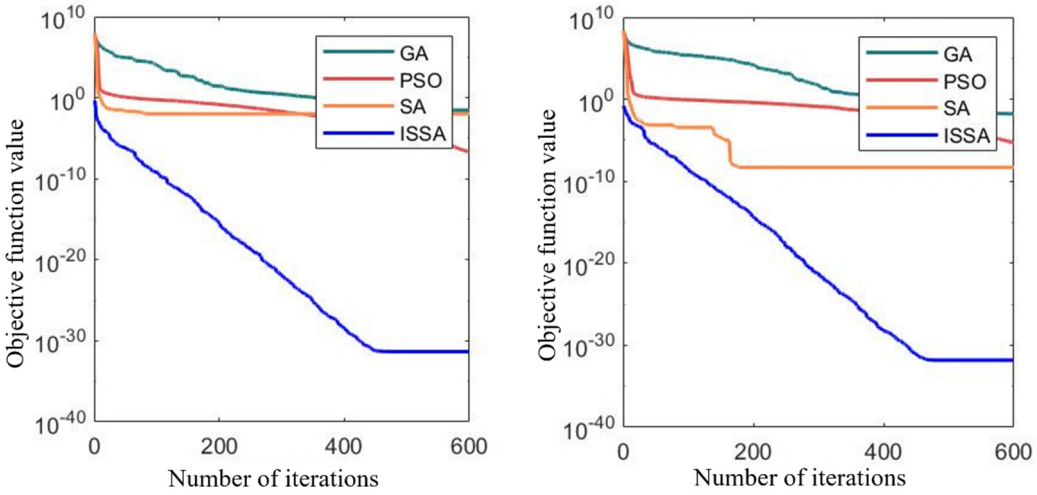


(**e**) Test function F_5.



(**f**) Test function F_6.

Figure 10. *Cont*.



(**g**) Test function F_7. (**h**) Test function F_8.

Figure 10. Algorithmic convergence graph.

Table 5. Multimodal test function.

Expression	Dimensionality	Initial Range	Theoretical Minimum
$F_5(x) = \sum_{i=1}^{n} \left[x_i^2 - 10\cos(2\pi x_i) + 10\right]$	30	$[-5.12, 5.12]$	0
$F_6(x) = -20\exp\left(-0.2\sqrt{\frac{1}{n}\sum_{i=1}^{n} x_i^2}\right) - \exp\left(\frac{1}{n}\sum_{i=1}^{n}\cos(2\pi x_i)\right) + 20 + \mathrm{e}$	30	$[-32, 32]$	0
$F_7(x) = \frac{\pi}{n}\left\{ \begin{array}{l} 10\sin(\pi y_i) + \sum_{i=1}^{n-1}(y_i-1)^2\left[1+10\sin^2(\pi y_{i+1})\right] \\ +(y_n-1)^2 \end{array} \right\} + \sum_{i=1}^{n} u(x_i, 10, 100, 4)$ $y_i = 1 + \frac{x_i+1}{4}$ $u(x_i, a, k, m) = \left\{ \begin{array}{l} k(x_i-a)^m, x_i > a \\ 0, -a < x_i < a \\ k(-x_i-a)^m, x_i < -a \end{array} \right.$	30	$[-50, 50]$	0
$F_8(x) = 0.1\left\{ \begin{array}{l} \sin^2(3\pi x_1) + \sum_{i=1}^{n}(x_i-1)^2\left[1+\sin^2(3\pi x_i+1)\right] \\ +(x_n-1)^2\left[1+\sin^2(2\pi x_n)\right] \end{array} \right\} + \sum_{i=1}^{n} u(x_i, 5, 100, 4)$	30	$[-50, 50]$	0

To avoid bias from a single run, each test function was simulated 30 times to acquire the optimal value (best), mean (mean), and standard deviation (Std) of the objective function. Smaller values indicate better algorithm performance. The mean represents the convergence accuracy, while Std indicates the stability and robustness of the algorithm. The results of the 30 trials were statistically analyzed. Table 6 presents the solutions obtained by the four different algorithms. Analysis of the data shows that for the selected eight test functions, the values calculated by ISSA are all smaller than those of the other three algorithms, proving that ISSA has relatively higher convergence accuracy and good stability and robustness.

Table 6. Comparison of algorithm test results.

Test Function	Statistical Value	GA	PSO	SA	ISSA
F_1	Best	0.0043057	3.8089×10^{-7}	1.8301×10^{-24}	1.7186×10^{-185}
	Mean	0.13229	4.3082×10^{-6}	1.2792×10^{-17}	8.2731×10^{-85}
	Std	0.14366	4.4473×10^{-6}	6.4957×10^{-17}	3.3865×10^{-84}
F_2	Best	0.011194	0.00033937	1.7639×10^{-15}	0
	Mean	0.07476	0.0019046	1.4181×10^{-12}	4.4503×10^{-43}
	Std	0.057258	0.0011043	2.2437×10^{-12}	1.8921×10^{-42}
F_3	Best	258.4487	0.0032469	1.4165	0
	Mean	2052.0915	0.030574	15.1909	3.3423×10^{-38}
	Std	1456.2121	0.027575	18.0307	1.83×10^{-37}
F_4	Best	0.54636	0.0062003	0.0003752	3.8004×10^{-104}
	Mean	2.0087	0.029958	0.002576	1.5277×10^{-29}
	Std	1.0917	0.016688	0.002755	8.3678×10^{-29}
F_5	Best	0.019599	3.68	0	0
	Mean	4.2203	11.8717	0.18468	0
	Std	2.7268	4.5515	0.45882	0
F_6	Best	0.35289	0.00028325	4.5208×10^{-13}	8.8818×10^{-16}
	Mean	14.7146	0.0024836	1.9116×10^{-9}	8.8818×10^{-16}
	Std	3.3813	0.0019813	9.5423×10^{-9}	0
F_7	Best	4.2088×10^{-5}	5.5344×10^{-9}	9.6221×10^{-25}	4.7116×10^{-32}
	Mean	0.048915	1.44×10^{-7}	2.5973×10^{-19}	4.7584×10^{-32}
	Std	0.14995	1.2898×10^{-7}	1.0855×10^{-18}	5.926×10^{-34}
F_8	Best	0.00012533	1.4425×10^{-7}	1.2179×10^{-24}	1.3498×10^{-32}
	Mean	0.010167	4.9289×10^{-6}	1.3983×10^{-18}	1.5675×10^{-32}
	Std	0.015147	8.0573×10^{-6}	5.3999×10^{-18}	3.4513×10^{-33}

3.4. Optimization of BP Neural Network by ISSA

Considering the drawbacks of random initialization in basic BP neural networks, it is necessary to use the ISSA with better performance to optimize the initial weights and thresholds. This brings the model parameters closer to optimal settings, thereby improving its generalization ability and prediction accuracy. Figure 11 shows the flowchart of the BP neural network prediction model optimized by ISSA. The optimization process is as follows:

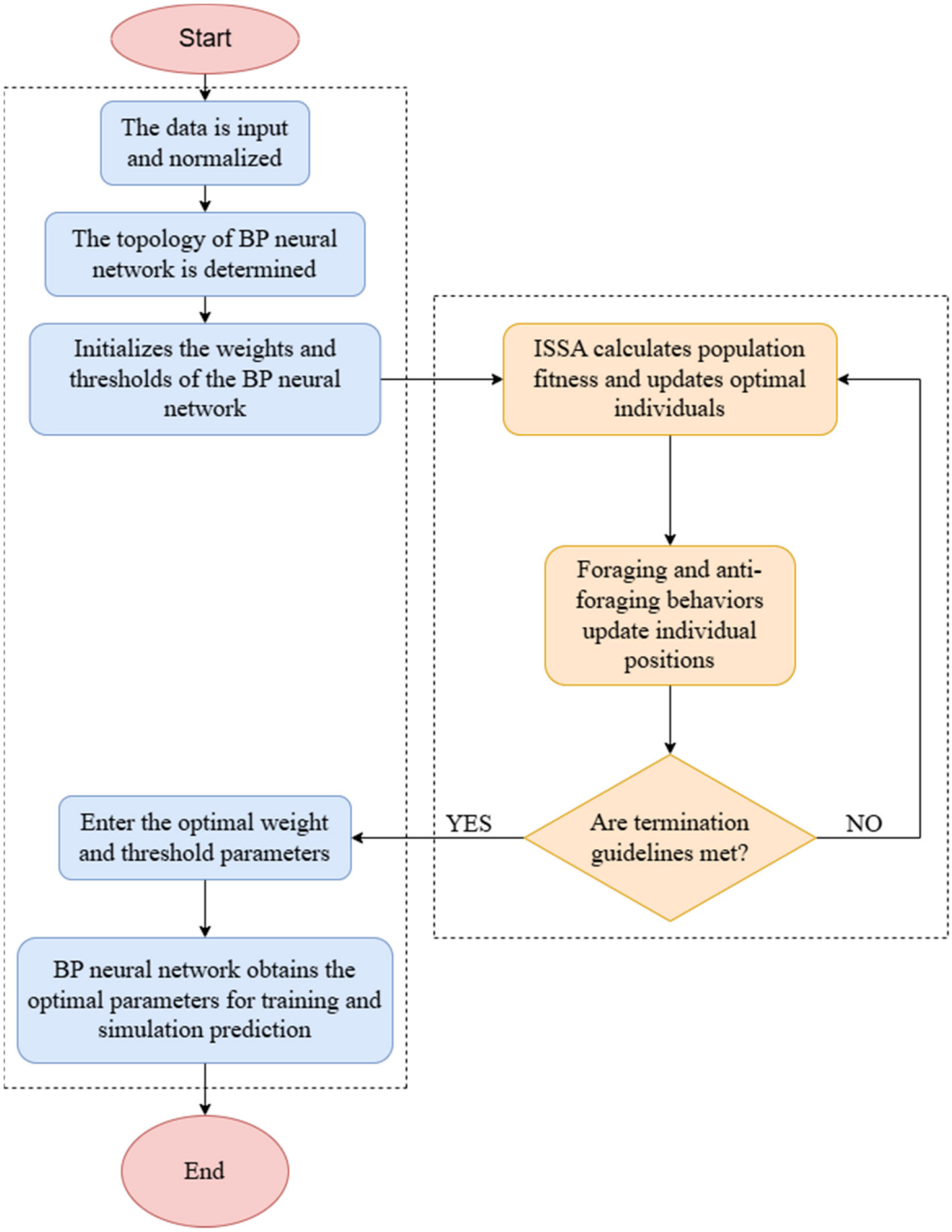
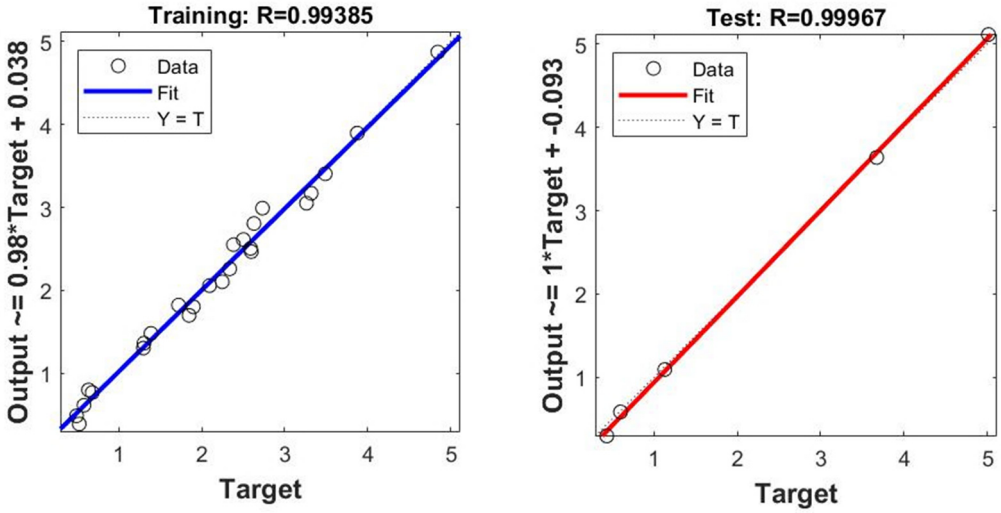


Figure 11. Flowchart of ISSA-BP algorithm.

First, the dataset obtained from the experiment was divided into training and test sets in 5:6 and 1:6 ratios and normalized. The topology and various parameters of the BP neural network were determined based on the method in Section 3.1. Then, the network's weights and thresholds were initialized, and the MSE of the training and test sets was selected as the fitness function for optimization. Next, the ISSA parameters were initialized, where the dimension matched the total number of network parameters. The ISSA was used to optimize the network's initial parameters, and the optimal parameters were output after the iterations were completed. Finally, the optimal initial weights and thresholds were assigned to the BP neural network for model training and prediction.

4. ISSA-BP Prediction Results and Error Analysis

To verify the prediction accuracy of the ISSA-BP neural network model, ISSA-BP was used to predict *Ra* in the dataset and compared with the traditional BP neural network and the SSA-BP neural network optimized by the basic sparrow search algorithm trained on the same dataset. The prediction values after training were compared with the true values and the prediction errors were calculated. The ISSA-BP neural network model established in this paper had three input layer nodes and one output layer node. During each training, the number of hidden layer nodes was optimized by comparing the mean square error (MSE) values of the model for different node numbers. The training effect of the model was judged based on correlation and multiple rounds of training were conducted until an optimal training result was obtained. As shown in Figure 12, the correlation of both the training and test sets was greater than 0.9, indicating that the training was relatively successful. The MSE values calculated for different hidden layer node numbers are shown in Table 7. The MSE value was minimized at 0.010231 when the number of hidden layer nodes was seven, so this was chosen as the optimal number of hidden layer nodes. It is worth noting that the MSE value when the number of nodes in the hidden layer was 11 had a larger gap compared to the other number of nodes, which may be due to the excessive complexity of the network, resulting in overfitting or local optimal solutions, making the training process unstable and the MSE abnormally large.



(**a**) Training set results. (**b**) Test set results.

Figure 12. Correlation analysis.

Table 7. The mean square error values for different numbers of hidden layer nodes.

Number of Nodes	MSE	Number of Nodes	MSE
3	0.021312	8	0.10216
4	0.018558	9	0.086325
5	0.013277	10	0.0619
6	0.025435	11	4.456
7	0.010231	12	0.07358

The improved ISSA-BP model, SSA-BP, and traditional BP neural networks were used to train and predict the experimental data, and the prediction results were compared. Table 8 shows the predicted values and error values of the three neural network models. Figure 13 presents the bar chart comparing the predicted and actual values, as well as the line chart of the error values for the three models. As seen in Figure 13, compared to the

other two prediction models, the predicted values of the ISSA-BP model are more closely aligned with the actual values, and its relative prediction error is smaller, demonstrating that the ISSA-BP prediction model has relatively higher accuracy in predicting the *Ra* value.

Table 8. Roughness *Ra* predicted value and error value.

	BP		SSA-BP		ISSA-BP	
True Value	**Predicted Value**	**Error Value**	**Predicted Value**	**Error Value**	**Predicted Value**	**Error Value**
1.387	1.203	−0.183	1.514	0.127	1.361	−0.025
3.875	4.267	0.392	4.246	0.371	4.050	0.175
0.679	1.035	0.356	0.978	0.299	0.609	−0.069
3.489	3.865	0.376	3.748	0.259	3.382	−0.106
1.592	1.817	0.225	1.711	0.119	1.587	−0.004
2.979	2.665	−0.313	3.152	0.173	2.961	−0.017
0.964	1.212	0.248	0.766	−0.197	1.017	0.053

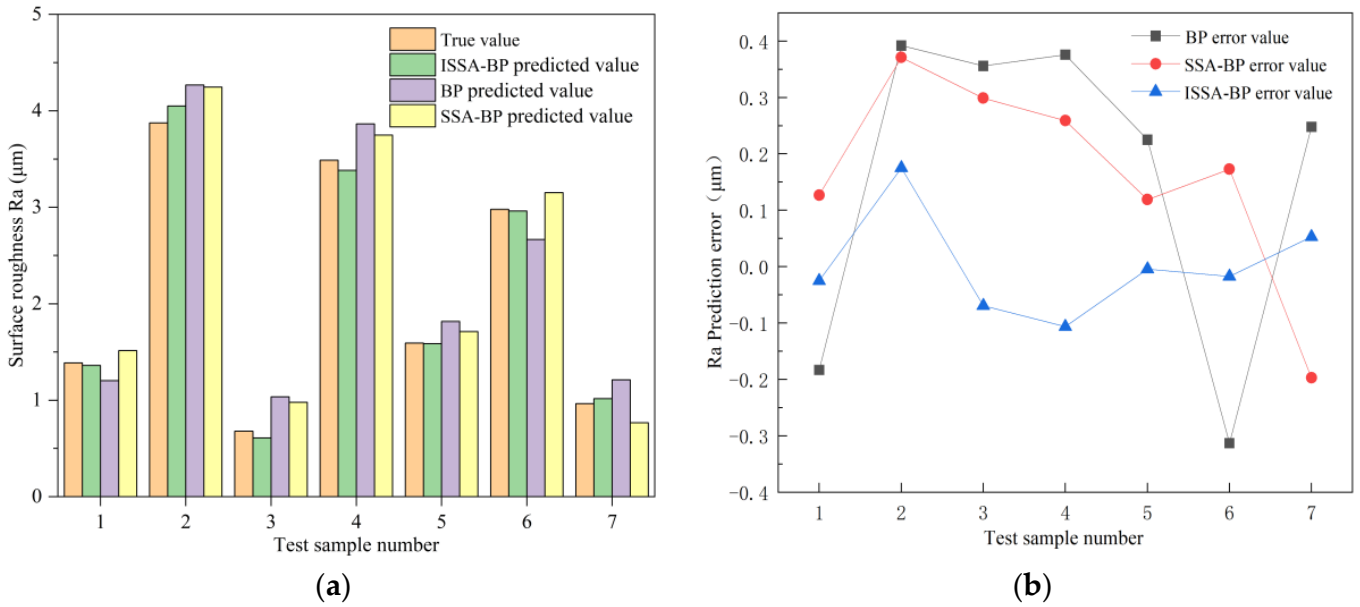


Figure 13. (**a**) The predicted *Ra* was compared with the true value using ISSA-BP, SSA-BP, and conventional BP neural networks on the prediction set; (**b**) *Ra* prediction error values of the three algorithms.

To evaluate the prediction performance of the optimized ISSA-BP model, four commonly used evaluation metrics were applied to comprehensively assess the regression prediction performance of the model: mean absolute error (MAE) (Equation (14)), MSE (Equation (6)), root mean square error (RMSE) (Equation (15)), and mean absolute percentage error (MAPE) (Equation (16)). The test results are shown in Table 9. From Table 9, it can be seen that the proposed ISSA-BP model outperforms the BP and SSA-BP prediction models across all evaluation metrics. Compared to the traditional BP model, the ISSA-BP model demonstrates significant optimization across various metrics. Specifically, it reduced MAE by 0.234965, MSE by 0.0880513, RMSE by 0.223652, and MAPE by 15.8709%. These results indicate that the ISSA-BP model greatly improves prediction accuracy. Compared to the traditional SSA-BP prediction model, the ISSA-BP model further enhances performance, lowering MAE by 0.156735, MSE by 0.0491513, RMSE by 0.152422, and MAPE by 11.1594%. This improvement highlights the potential of the ISSA-BP model to enhance prediction accuracy and reliability in practical applications, especially when handling complex data.

The model effectively reduces errors and increases prediction stability. These comparisons of the error metrics demonstrate that the ISSA-BP prediction model has better prediction accuracy.

$$MAE = \frac{1}{n}\sum_{i=1}^{n}\left|\hat{y}_i - y_i\right| \tag{14}$$

$$RMSE = \sqrt{\frac{1}{n}\sum_{i=1}^{n}\left(\hat{y}_i - y_i\right)^2} \tag{15}$$

$$MAPE = \frac{1}{n}\sum_{i=1}^{n}\left|\frac{\hat{y}_i - y_i}{y_i}\right| \times 100\% \tag{16}$$

where n is the number of samples, $\hat{y}_i$ is the predicted value, and y_i is the true value.

Table 9. Prediction error value.

	Error Type	BP	SSA-BP	ISSA-BP
R_a	MAE	0.29944	0.22121	0.064475
	MSE	0.095281	0.056381	0.0072297
	RMSE	0.30868	0.23745	0.085028
	MAPE	19.588%	14.8765%	3.7171%

5. Conclusions

This paper proposes an ISSA-BP prediction model based on an improved sparrow search algorithm to predict the surface roughness of NdFeB material in diamond wire sawing. Based on experimental data, the effects of feed speed, wire speed, and workpiece size on the surface morphology and roughness of NdFeB material were analyzed. The following conclusions were drawn from the study:

(1) Within the range of the process parameters studied in this paper, the sawed surface morphology of NdFeB shows the combined effects of brittle removal and ductile removal. As the feed speed and workpiece size decrease and the wire speed increases, the proportion of the ductile removal area on the sawn material surface gradually increases.

(2) Within the range of process parameters studied in this paper, the *Ra* of NdFeB during sawing ranged from 0.433 μm to 5.015 μm. Both feed speed and workpiece size are directly proportional to surface roughness, while wire speed is inversely proportional to it. Among these, feed speed is the most significant factor affecting SR, followed by wire speed, with workpiece size having the least effect.

(3) By introducing Cubic chaotic mapping, Latin hypercube sampling, the sine–cosine algorithm, Levy flight, and Cauchy mutation to improve the traditional sparrow search algorithm (SSA), the resulting ISSA outperformed the GA, SA, and PSO algorithms in the optimization performance of the eight test functions. It exhibited faster convergence and better optimization performance.

(4) The ISSA-BP prediction model is obtained by optimizing the BP neural network using the improved ISSA. Compared to SSA-BP and traditional BP models, ISSA-BP significantly reduces error metrics, achieving an MAE of 0.064475, MSE of 0.0072297, RMSE of 0.085028, and MAPE of 3.7171%. These results demonstrate its higher prediction accuracy and better generalization ability.

Author Contributions: G.L.: investigation, writing—original draft preparation, data curation. X.Z.: investigation, methodology, writing—original draft preparation. Y.G.: conceptualization, writing—review and editing, project administration, funding acquisition. F.C.: methodology. Z.S.: funding acquisition. All authors have read and agreed to the published version of the manuscript.

Funding: The work was financially supported by the National Key Research and Development Project (no. 2022YFB3401902) and Natural Science Foundation of Shandong Province (no. ZR2023ME145).

Data Availability Statement: The original contributions presented in this study are included in the article. Further inquiries can be directed to the corresponding author.

Conflicts of Interest: The authors declare no conflicts of interest.

References

1. Liang, S.; Shao, X.; Que, Y.; Guo, B.; Bao, H.; Tang, G.; Yan, X.; Bao, J.; Yang, L.; Qin, L.; et al. Recent advances in mechanical properties of sintered NdFeB magnets. *J. Alloys. Compd.* **2024**, *1003*, 175689. [CrossRef]
2. Zhang, X.; Gao, Y.; Yang, C.; Shi, Z. Surface Characteristics of Precision As-Cut NdFeB Magnet Considering Diamond Wire Wear. *Precis. Eng.* **2024**, *89*, 23–36. [CrossRef]
3. Coey, J. Perspective and prospects for rare earth permanent magnets. *Engineering* **2020**, *6*, 119–131. [CrossRef]
4. Wang, S.; Yan, X.; Xue, F.; Dong, D.; Zhang, X.; Ma, F.; Wang, H.; Lv, Y. Fast magnetic reconstruction of the portal vein with allogeneic blood vessels in canines. Hepatobiliary. *Pancreat. Dis. Int.* **2015**, *14*, 293–299. [CrossRef]
5. Liu, J.; Zhang, Z.; Wan, S.; Wu, B.; Feng, J.; Zhang, T.; Zhou, C. Experimental and theoretical investigations on diamond wire sawing for a NdFeB magnet. *Materials* **2022**, *15*, 3034. [CrossRef]
6. Wu, B.; Zhang, Z.; Feng, J.; Meng, F.; Wan, S.; Zhuang, X.; Li, L.; Liu, H.; Zhang, F. Experimental investigation on the surface formation mechanism of NdFeB during diamond wire sawing. *Materials* **2023**, *16*, 1521. [CrossRef]
7. Pala, U.; Kuster, F.; Wegener, K. Characterization of electroplated diamond wires and the resulting workpiece quality in silicon sawing. *J. Mater. Process. Technol.* **2020**, *276*, 116390. [CrossRef]
8. Gao, P.; Tan, B.; Yang, F.; Li, H.; Bian, N.; Sun, X.; Liu, M.; Wang, R. Influence of diamond wire saw slicing parameters on (010) lattice plane beta-gallium oxide single crystal wafer. *Mater. Sci. Semicond. Process.* **2021**, *133*, 105939. [CrossRef]
9. Costa, E.; Weingaertner, W.; Xavier, F. Influence of single diamond wire sawing of photovoltaic monocrystalline silicon on the feed force, surface roughness and micro-crack depth. *Mater. Sci. Semicond. Process.* **2022**, *143*, 106525. [CrossRef]
10. Yin, Y.; Gao, Y.; Li, X.; Pu, T.; Wang, L. Experimental study on slicing photovoltaic polycrystalline silicon with diamond wire saw. *Mater. Sci. Semicond. Process.* **2020**, *106*, 104779. [CrossRef]
11. Azami, A.; Khoshanjam, A.; Jerez-Mesa, R.; Lluma-Fuentes, J.; Travieso-Rodriguez, J. A new theoretical model for surface roughness prediction in rotational abrasive finishing process. *Wear* **2023**, *524–525*, 204772. [CrossRef]
12. Jia, J.; Ma, L.; Sun, Y.; Tang, B.; Jiang, Y.; Li, M.; Tan, Y. Research on the mechanism of tool-workpiece coupling contact and theoretical modeling of surface roughness in turning brittle materials. *Int. J. Adv. Manuf. Technol.* **2024**, *134*, 4201–4214. [CrossRef]
13. Jing, X.; Song, B.; Xu, J.; Zhang, D. Mathematical modeling and experimental verification of surface roughness in micro-end-milling. *Int. J. Adv. Manuf. Technol.* **2022**, *120*, 7627–7637. [CrossRef]
14. Li, X.; Gao, Y.; Yin, Y.; Wang, L.; Pu, T. Experiment and theoretical prediction for surface roughness of PV polycrystalline silicon wafer in electroplated diamond wire sawing. *J. Manuf. Process.* **2020**, *49*, 82–93. [CrossRef]
15. Zhu, Z.; Gao, Y. Study on surface roughness and morphology of diamond wire as-sawn sapphire crystal wafers. *Int. J. Adv. Manuf. Technol.* **2023**, *125*, 2077–2090. [CrossRef]
16. Upadhyay, V.; Jain, P.; Mehta, N. In-process prediction of surface roughness in turning of Ti–6Al–4V alloy using cutting parameters and vibration signals. *Measurement* **2013**, *46*, 154–160. [CrossRef]
17. Ozturk, S.; Aydin, L.; Celik, E. A comprehensive study on slicing processes optimization of silicon ingot for photovoltaic applications. *Sol. Energy* **2018**, *161*, 109–124. [CrossRef]
18. Kayabasi, E.; Ozturk, S.; Celik, E.; Kurt, H. Determination of cutting parameters for silicon wafer with a diamond wire saw using an artificial neural network. *Sol. Energy* **2017**, *149*, 285–293. [CrossRef]
19. Aiyar, H.; Chauhan, G.; Gupta, N. Soft modeling of WEDM process in prediction of surface roughness using artificial neural networks. In *Recent Advances in Smart Manufacturing and Materials*; Springer: Singapore, 2021; pp. 465–474. [CrossRef]
20. Paturi, U.; Devarasetti, H.; Reddy, N.S.; Kotkunde, N.; Patle, B. Modeling of surface roughness in wire electrical discharge machining of Inconel 718 using artificial neural network. *Mater. Today Proc.* **2021**, *38*, 3142–3148. [CrossRef]
21. Boga, C.; Koroglu, T. Proper estimation of surface roughness using hybrid intelligence based on artificial neural network and genetic algorithm. *J. Manuf. Process.* **2021**, *70*, 560–569. [CrossRef]
22. Yang, H.; Li, X.; Qiang, W.; Zhao, Y.; Zhang, W.; Tang, C. A network traffic forecasting method based on SA optimized ARIMA–BP neural network. *Comput. Netw.* **2021**, *193*, 108102. [CrossRef]
23. Liu, L.; Xiong, H.; Lu, Y. Multi-beam sonar elevation data prediction based on optimized BP neural network. In Proceedings of the 2022 IEEE 6th Information Technology and Mechatronics Engineering Conference (ITOEC), Chongqing, China, 4–6 March 2022; pp. 883–888. [CrossRef]

24. Cui, F.; Wang, H.; Shu, Z. Prediction of aerodynamic pressure amplitude in tunnel based on PSO-BP neural network. *J. Cent. South. Univ. Sci. Technol.* **2023**, *54*, 3752–3761. [CrossRef]
25. Wang, J.; Chen, B.; Yang, W.; Xu, D.; Yan, B.; Zou, E. BP neural network multi-module green roof thermal performance prediction model optimized based on sparrow search algorithm. *J. Build. Eng.* **2024**, *96*, 110615. [CrossRef]
26. Yu, X.; Luo, L. Day-ahead wind power prediction based on BP neural network optimized by improved sparrow search algorithm. In Proceedings of the 2022 4th Asia Energy and Electrical Engineering Symposium (AEEES), Chengdu, China, 25–28 March 2022; pp. 230–235. [CrossRef]
27. Zheng, Y.; Li, L.; Qian, L.; Cheng, B.; Hou, W.; Zhuang, Y. Sine-SSA-BP ship trajectory prediction based on chaotic mapping improved sparrow search algorithm. *Sensors* **2023**, *23*, 704. [CrossRef]
28. Lawn, B.; Evans, A.; Marshall, D. Elastic/plastic indentation damage in ceramics: The median/radial crack system. *J. Am. Ceram. Soc.* **1980**, *63*, 574–581. [CrossRef]
29. Marshall, D.B.; Lawn, B.; Evans, A. Elastic/plastic indentation damage in ceramics: The lateral crack system. *J. Am. Ceram. Soc.* **1982**, *65*, 561–566. [CrossRef]
30. Huang, H.; Zhang, Y.; Xu, X. Experimental investigation on the machining characteristics of single-crystal SiC sawing with the fixed diamond wire. *Int. J. Adv. Manuf. Technol.* **2015**, *81*, 955–965. [CrossRef]
31. Wu, H. Wire sawing technology: A state-of-the-art review. *Precis. Eng.* **2016**, *43*, 1–9. [CrossRef]
32. Xing, Q.; Yao, Z.; Zhang, Q. Effects of processing parameters on processing performances of ultrasonic vibration-assisted micro-EDM. *Int. J. Adv. Manuf. Technol.* **2021**, *112*, 71–86. [CrossRef]
33. Saif, M.; Tiwari, S. Investigation towards surface roughness & material removal rate in wire-EDM of aluminium alloy 6061 and 5083 using Taguchi method. *Mater. Today Proc.* **2021**, *47*, 1040–1047. [CrossRef]
34. Hornik, K. Approximation capabilities of multilayer feedforward networks. *Neural Netw.* **1991**, *4*, 251–257. [CrossRef]
35. Pan, X.; Niu, Y.; Zhao, Y.; Huang, P.; Wu, Y. Parameter calibration method of clustered-particle logic concrete DEM model using BP neural network-particle swarm optimisation algorithm (BP-PSO) inversion method. *Eng. Fract. Mech.* **2023**, *292*, 109659. [CrossRef]
36. Bao, X.; Ying, J.; Cheng, F.; Zhang, J.; Luo, B.; Li, L.; Liu, H. Research on neural network model of surface roughness in belt sanding process for Pinus koraiensis. *Measurement* **2018**, *115*, 11–18. [CrossRef]
37. Xue, J.; Shen, B. A novel swarm intelligence optimization approach: Sparrow search algorithm. *Syst. Sci. Control Eng.* **2020**, *8*, 22–34. [CrossRef]
38. Yu, H.; Fan, G.; Zhang, G.; Wang, W.; Li, Y.; Zhang, S.; Li, B. Regression model of rotor shape errors based on the ISSA-BP neural network. *J. Mech. Sci. Technol.* **2024**, *38*, 1925–1938. [CrossRef]
39. Zhang, B.; Liu, W.; Cai, Y.; Zhou, Z.; Wang, L.; Liao, Q.; Fu, Z.; Cheng, Z. State of health prediction of lithium-ion batteries using particle swarm optimization with Levy flight and generalized opposition-based learning. *J. Energy Storage* **2024**, *84*, 110816. [CrossRef]
40. Li, T.; Zhang, W.; Mi, K.; Lin, Q.; Zhao, S.; Song, J. Fault diagnosis method of energy storage unit of circuit breakers based on EWT-ISSA-BP. *Energy Eng.* **2024**, *121*, 1991–2007. [CrossRef]
41. Yao, X.; Liu, Y.; Lin, Y.; Lin, G. Evolutionary programming made faster. *IEEE Trans. Evol. Comput.* **1999**, *3*, 82–102. [CrossRef]

Disclaimer/Publisher's Note: The statements, opinions and data contained in all publications are solely those of the individual author(s) and contributor(s) and not of MDPI and/or the editor(s). MDPI and/or the editor(s) disclaim responsibility for any injury to people or property resulting from any ideas, methods, instructions or products referred to in the content.